ISSN 1330-3651 (Print), ISSN 1848-6339 (Online)
Received: 29 July 2025; Accepted: 16 October 2025

https://doi.org/10.17559/TV-20250729002870
Original scientific paper

An Experimental and Simulation Study of Ultrasonic-Assisted MIG Welding Power Supply

Borui LU, Bojin QI*

Abstract: This paper presents the design and control of a digitally regulated MIG welding power supply capable of superimposing ultrasonic-frequency current (20-100 kHz) onto a low-frequency pulsed current (0-500 A, 10 ms period). The proposed topology employs a full-bridge inverter at the primary stage and three Buck converters at the secondary stage, with IGBT modules as switching devices. To ensure stable high-frequency operation, an active snubber and energy feedback circuit are integrated. The control system, implemented on an STM32 microcontroller with PI-based closed-loop regulation, enables flexible waveform modulation and precise current control. System parameters were optimized in MATLAB/Simulink and validated experimentally. Results demonstrate accurate generation of complex current waveforms and improved stability of droplet transfer compared with conventional power supplies. The developed system provides a viable solution for next-generation MIG welding applications requiring high efficiency, reduced spatter, and controllable heat input.

Keywords: buck circuit; control strategy; simulation analysis; ultrasonic pulses; welding power supply

1 INTRODUCTION

Although conventional MIG welding technology has been extensively utilized in industrial manufacturing, it continues to face significant challenges such as unstable arc characteristics, irregular droplet transfer, and excessive spatter generation, all of which constrain the advancement of welding processes [1]. With the global manufacturing industry undergoing a paradigm shift toward higher precision, efficiency, and automation [2], welding - being a core fabrication technology - is subject to increasingly stringent performance requirements. As a result, achieving active, precise, and fully digital control of the welding process has become essential for overcoming the inherent limitations of traditional techniques. This evolution places greater demands on the design and functionality of welding power supplies, necessitating innovations in control strategies, waveform generation, and system integration.

To address the limitations of conventional welding power supplies that primarily deliver low-frequency current output, this paper proposes a novel ultrasonic superimposed pulsed MIG welding power supply architecture. The system introduces a set of advanced waveform output strategies by superimposing a 20-100 kHz ultrasonic-frequency current (0-100 A) onto a conventional low-frequency pulsed current (0-500 A). Control is realized through digital waveform modulation combined with an improved PI regulation circuit, while circuit configuration and control parameters are optimized using MATLAB/Simulink-based simulation. At the hardware level, the power supply integrates dual Buck converters dedicated to ultrasonic current generation, enabling flexible superposition of diverse ultrasonic current waveforms with precise regulation. The proposed design is expected to significantly enhance droplet transfer stability, reduce spatter, and optimize weld pool dynamics, thereby providing a new technical pathway for improving the quality and efficiency of pulsed MIG welding processes.

2 LITERATURE REVIEW

In recent years, various external stimuli such as magnetic fields [3, 4], acoustic waves [5], lasers [6], and pulsed currents [7] have been integrated into pulsed MIG welding processes to improve droplet transfer behavior and enhance the overall performance of welding power supplies. From the perspective of current waveform control, several techniques have been proposed, including double-pulsed MIG welding [8, 9], twin-wire sinusoidal modulation [10, 11], and symmetrical waveform transition control [12]. However, these approaches are predominantly limited to low-frequency operation, typically around 100 Hz, which restricts their effectiveness in meeting the many demands of next-generation high-speed, high-precision welding applications.

Simultaneously, advances in power electronics technology have been progressively integrated into welding power supply systems, leading to significant improvements in pulsed MIG power supply performance and enabling the industrialization and commercialization of advanced welding equipment. A notable example is the Cold Metal Transfer (CMT) welding technology, developed by the Austrian company Fronius in 2002 [13-15], which represents a major breakthrough in arc welding by offering precise control of heat input and droplet transfer. With years of technological accumulation, welding process specification parameters and expert knowledge databases have been increasingly embedded into modern welding power supplies, enabling unified and intelligent control. Concurrently, precise regulation of welding current waveforms allows stable adaptation to varying plate thicknesses, wire diameters, and material types. Compared with conventional gas metal arc welding (GMAW), Cold Metal Transfer (CMT) welding offers significantly lower heat input and a more stable droplet transfer process. Since its introduction, CMT technology has rapidly gained widespread adoption across various industrial sectors due to its superior performance. It has been particularly effective in the welding of thin plates, as well as materials such as aluminum [16], copper, and dissimilar metal joints [13, 17]. In the field of arc additive manufacturing, the low heat input characteristic of CMT technology can be effectively combined with the near-immersion active cooling (NIAC) method to enhance thermal management, thereby reducing heat accumulation and overcoming limitations related to deposition cycles, complex geometries, and anisotropic mechanical properties [18, 19]. However, in the early stages of welding power supply

development, many research and development organizations lacked sufficient experience and industry-specific knowledge, resulting in significant challenges in establishing a comprehensive and optimized process database.

Despite these fundamental challenges, technological innovation in the field of welding power supplies continues to advance rapidly. With the rapid development of the semiconductor industry, welding power supply research is increasingly leveraging breakthroughs from adjacent fields. In particular, new high-power switching devices such as silicon carbide (SiC) semiconductors are gradually being introduced and applied in welding power systems, [20-24]. These devices are capable of switching at frequencies up to 100 kHz, offering significant potential for high-frequency power and enhanced power system performance. However, in practical applications, the dynamic response characteristics of these devices - especially under high-frequency operating conditions - limit the achievable output current waveform, with the effective maximum frequency of combined pulse current typically constrained to approximately 30 kHz.

Accordingly, this paper seeks to demonstrate that, through optimized topology and digital control, current semiconductor devices can be fully leveraged to achieve high-frequency current generation, offering new opportunities for performance enhancement in pulsed MIG welding systems.

3 RESEARCH METHODOLOGY

3.1 Development of the Power Supply Unit

The ultrasonic-assisted pulsed MIG welding power supply developed in this study is composed of two main sections: a front-end constant-voltage source and a rear-end composite current output stage.

(1) Front-end circuit, as illustrated in Fig. 1a: The system is supplied by a 380 V three-phase AC input (three-phase plus neutral).

Rectification: The input is first rectified by a three-phase rectifier module, producing a DC bus voltage of approximately 540 V.

DC-DC conversion: The rectified voltage is processed by a full-bridge (H-bridge) converter operating at 20 kHz, and then stepped down by a high-frequency transformer with a 5:1 turns ratio, yielding a stable load voltage of about 105 V.

Voltage regulation: A closed-loop feedback circuit dynamically adjusts the duty cycle of the IGBT drive signals in response to load variations, thereby maintaining a constant output voltage.

Protection: To safeguard the switching devices against short-circuit faults, the gate driver chips are equipped with built-in desaturation (DESAT) detection. If an abnormal rise in the IGBT collector-emitter voltage (V_{ce}) is detected, the driver immediately identifies a short-circuit or overcurrent fault and initiates a fast hardware-level shutdown.

The full-bridge stage is implemented using IGBTs, selected for their superior performance in high-current applications. Although IGBTs generally exhibit higher on-resistance than MOSFETs, their conductivity modulation effect under large currents significantly reduces conduction losses, which is critical for high-power welding applications requiring high efficiency and reliable thermal performance.

(2) Rear-end circuit, as illustrated in Fig. 1b: The regulated DC output from the front-end stage serves as the input to the rear-end circuit, which adopts a Buck topology (also referred to as a step-down converter), as shown in Fig. 1b. The Buck converter is a well-established DC-DC architecture widely used for its simplicity, high efficiency, and suitability for generating stable low-voltage outputs [25]. In this design: The first Buck channel provides a low frequency pulsed current output. The second and third Buck channels generate ultrasonic-frequency currents in the range of 20-100 kHz. By superimposing the outputs of these circuits, the system achieves flexible generation of composite current waveforms, enabling precise control of both low-frequency and ultrasonic-assisted components.

To achieve controllable amplitude levels for both low-frequency and high-frequency pulse currents, precise regulation of several key parameters is required during the low-frequency pulse stage. These parameters include the base current amplitude and duration, the peak current amplitude and duration, as well as the amplitude, frequency, and duty cycle of the high-frequency current superimposed on each low-frequency pulse segment. Realization of such multi-parameter control necessitates dedicated circuitry capable of accurately generating and coordinating the desired current waveforms.

As shown in Fig. 1b, the power supply system adopts the STM32G474VE microcontroller (MCU) as the central control unit. The MCU generates the target current references, denoted as I_{g1}, I_{g2} and I_{g3}. Correspondingly, the actual low-frequency current signals, I_{f1}, I_{f2} and I_{f3}, are measured by current sensors and conditioned through an operational amplifier circuit for proportional-integral (PI) control. The resulting error signals modulate the pulse-width modulation (PWM) signals of the driver circuit, thereby adjusting the switching duration of the IGBTs. This configuration enables closed-loop regulation of current amplitude, ensuring accuracy and fast response during operation.

During high-frequency switching, the terminals of the power transistors are susceptible to voltage spikes and parasitic charge accumulation. These effects not only accelerate device degradation but also distort the high-frequency current waveform. To mitigate this problem, the proposed power supply integrates an absorption and feedback circuit that captures voltage spikes and parasitic charges and redirects the recovered energy to the output capacitor of the upstream stage.

As shown in Fig. 1c, PWM signals from P2± and P1± alternately drive the IGBTs to perform switching operations. The voltage spikes generated at the Buck output stage are rectified by transistors S8 and S9 configured in a half-bridge arrangement. The rectified signals are then converted into alternating voltages and transferred through a transformer for voltage scaling. Finally, the transformed voltage is rectified and fed back to the main circuit of the preceding stage via a rectifier bridge, thereby achieving energy recovery and improving overall power conversion efficiency.

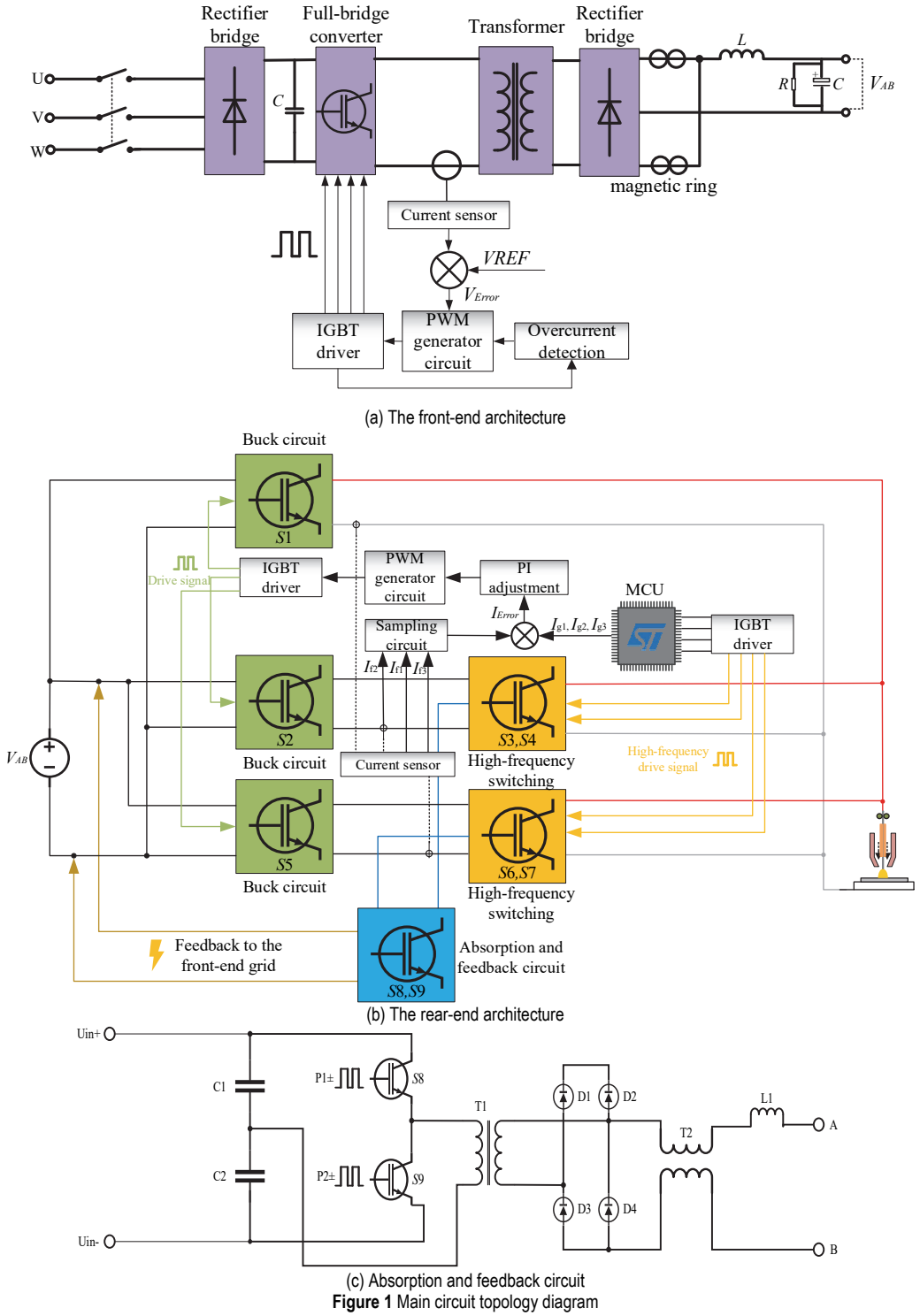

Figure 1 Main circuit topology diagram

3.2 Working Modes and Principles

To superimpose ultrasonic currents onto the base and peak stages of the low-frequency pulse, three Buck converters are employed. Based on the principle of current superposition, this configuration generates the low-frequency base current (I_A), the high-frequency base pulse current (I_{bp}), and the high-frequency peak pulse current (I_{pp}) can be flexibly combined to form the desired output waveform

Both the low-frequency pulse circuit and the high-frequency front-end circuits are implemented using Buck converters. The power switches, IGBTs *S*1, *S*4, and *S*5, are driven by PWM signals generated through a proportional-integral (PI) regulator. Among them, *S*1 is dynamically modulated according to the reference current I_{g1} provided by the microcontroller at different operating stages. The low-frequency circuit delivers a base pulse current (I_A) up to 100Hz, while the Buck converters in the high-frequency front-end generate constant currents, denoted as I_C and I_D.

The ultrasonic currents in the 20-100 kHz range are generated using a Buck converter topology. At the output stage, the IGBT switches are alternately commutated under microcontroller control, with the switching frequency and duty cycle precisely defined to produce the desired high-frequency output. Specifically, when switch *S*3 (or *S*6) is

turned ON while *S*4 (or *S*7) remains OFF, the constant current produced by the front-end Buck circuit is short-circuited back to the main circuit, thereby reducing the output current to zero. Conversely, when switch *S*3 (or *S*6) is turned OFF while *S*4 (or *S*7) is turned ON, the constant current generated by the upstream Buck circuit is directed to the welding gun load.

The periodic commutation of switches *S*3, *S*4, *S*6, and *S*7 is governed by the PWM signals originating from the microcontroller. This action generates high-frequency pulse currents whose frequency and duty cycle correspond directly to those of the microcontroller's PWM waveform. The amplitude of the resultant pulse current is determined by the magnitude of the current output from the preceding Buck circuit.

It should be noted that the high-frequency switching of IGBTs and similar power devices inherently generates electromagnetic radiation, making electromagnetic interference (EMI) suppressiona critical design consideration. To address this, magnetic rings are integrated into the circuit to attenuate the EMI produced by the high-frequency operation of the IGBTs in the main stage.

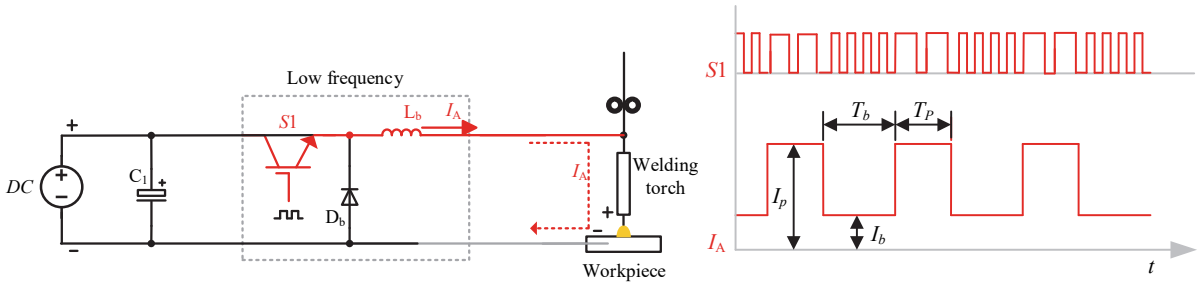

(a) Low-frequency current pulse circuit; (b) Low-frequency pulse mode IGBT operation and current waveform

Figure 2 Low-frequency pulse mode

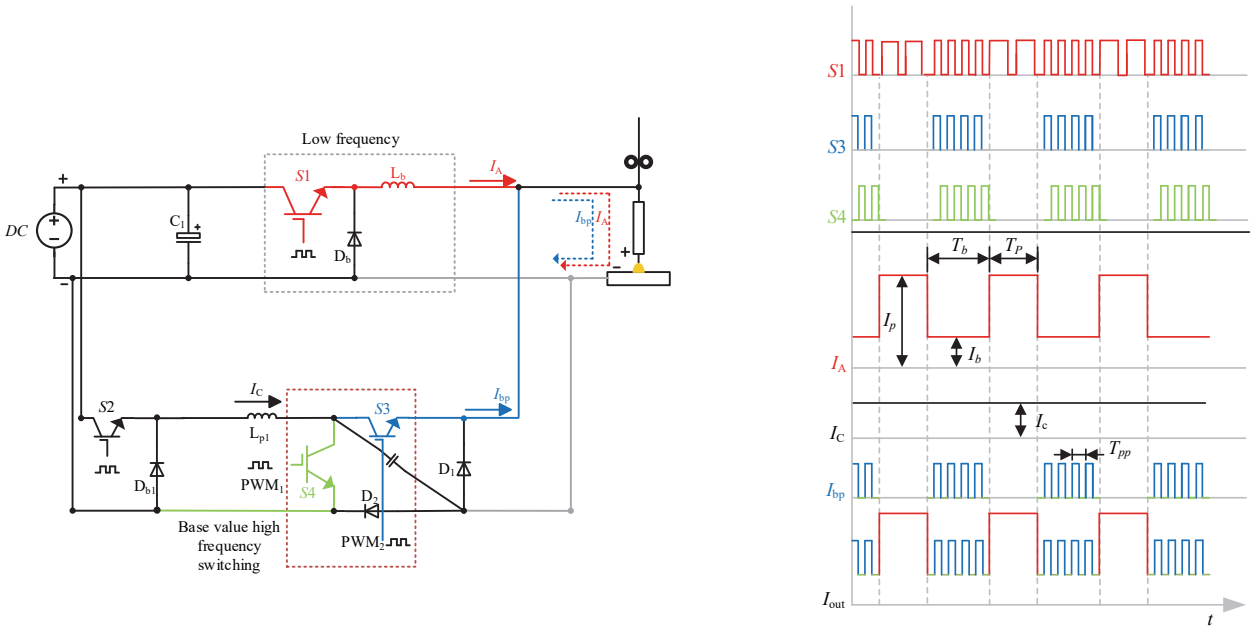

(a) Low-frequency and base-value high-frequency circuits; (b) Base-value ultrasonic mode IGBTs operation and current waveform

Figure 3 Base-value ultrasonic mode

(a) Low-frequency pulse mode

As illustrated in Fig. 2, the high-frequency circuits are inactive in this operating mode, and only the low-frequency base-value circuit remains active. Switch *S*1 is regulated by a closed-loop control system that modulates its PWM signal. During the base-value interval (T_b), the microcontroller sets the current reference Ig1 to the base current level I_b. In the subsequent peak interval (T_p), Ig1 is elevated to the peak current level I_p. As a result, the duty cycle of the PWM signal applied to *S*1 increases in the peak phase compared to the base phase.

The operational parameters are specified as follows: the base interval T_b is adjustable within 10-150 ms, while the peak interval T_p ranges from 10-100 ms. The peak current I_p can reach up to 500 A, and the operating frequency of the low-frequency current is tunable from 0 to 100 Hz.

(b) Base-value ultrasonic mode

The base-value low-frequency current I_A exhibits a pulsed output characteristic corresponding to the low-frequency pulse mode, as illustrated in Fig. 3. The gate signal I_{g2}, configured by the microcontroller, is set to the constant current level I_c, which drives the preceding Buck converter to produce a constant output current with a maximum amplitude of 100 A. The high-frequency current component during the base-value phase, denoted as I_{bp}, is superimposed onto this low-frequency pulse.

During the base-value interval T_b, the base-value high-

frequency circuit is activated. In this mode, the pre-stage circuit, controlled by switch $S2$, delivers a constant current I_c, while the post-stage switching network - comprising switches $S3$ and $S4$ - alternates between conduction and cut off at a frequency and duty cycle specified by the microcontroller, thereby generating the high-frequency current I_{bp}. In contrast, during the peak interval T_p, the Buck-stage switch $S2$ of the base-value high-frequency circuit is deactivated. According to Kirchhoff's Current Law (KCL), the high-frequency currents generated during the base and peak intervals are superimposed with the low-frequency pulse current, yielding the final composite output current I_{out}.

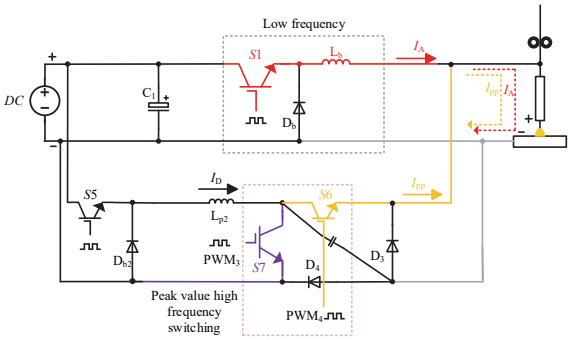

(a) Low-frequency and peak-value high-frequency circuits

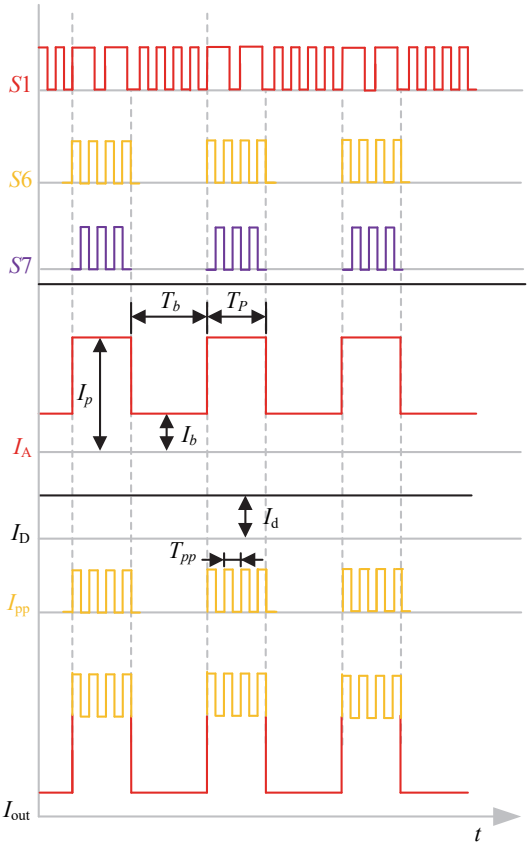

(b) Peak-value ultrasonic mode IGBTs operation and current waveform

Figure 4 Peak-value ultrasonic mode

(c) Peak-value ultrasonic mode

The control signal I_{g3} is configured to deliver the peak current I_d, driving the pre-stage Buck converter of the peak high-frequency pulse circuit to generate a constant current I_D with a maximum output of 100 A, as illustrated in Fig. 4b. The high-frequency current component during the peak phase, denoted as I_{pp}, is thereby introduced.

During the peak interval T_p, the peak high-frequency circuit is activated. As shown in Fig. 4a, the pre-stage circuit, controlled by switch $S5$, provides the constant current I_d. In the post-stage switching network, switches $S6$ and $S7$ alternate between conduction and cut off at the specified switching frequency and duty cycle, thereby generating the high-frequency current I_{pp}. This current is superimposed on the low-frequency pulse current, resulting in the composite output current I_{out}.

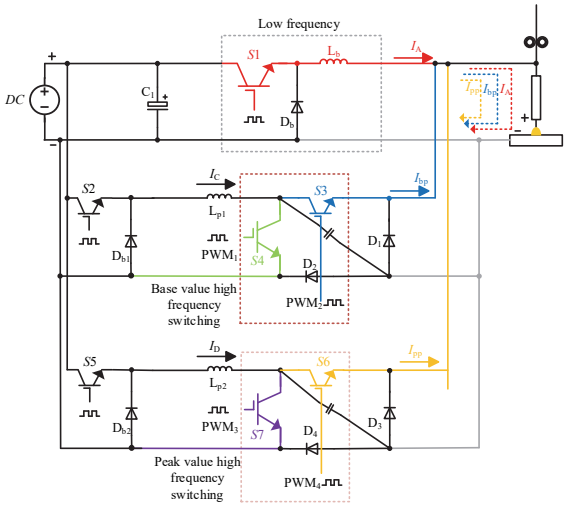

(a) Low-frequency and base-peak-value high-frequency circuits

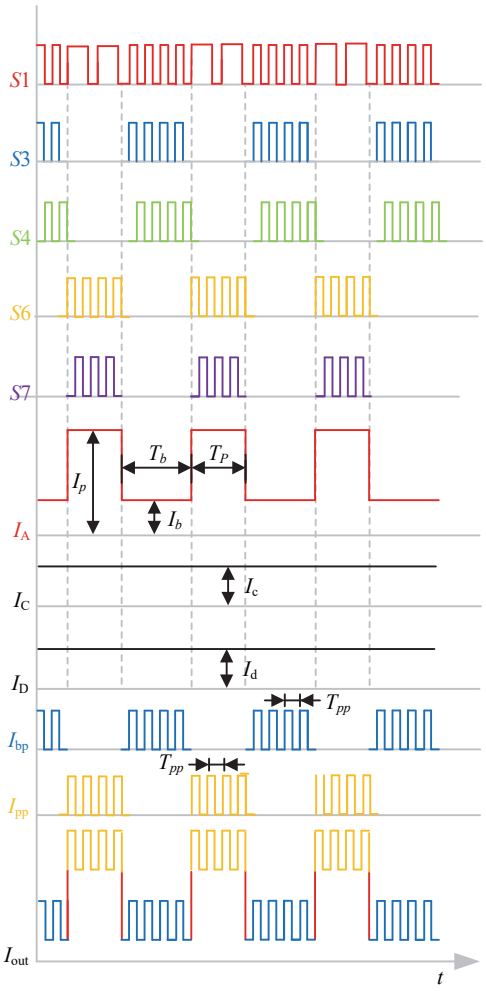

(b) Combined ultrasonic mode IGBTs operation and current waveform

Figure 5 Combined ultrasonic mode

(d) Combined ultrasonic mode

During the base interval T_b, the control circuit sets reference signal I_{g2} to I_c and I_{g3} to zero. As shown in Fig. 5, switches $S3$ and $S4$ alternate between conduction and cutoff at the prescribed switching frequency and duty cycle, thereby generating the high-frequency current component I_{bp}. During the peak interval T_p, the control circuit sets I_{g3} to I_d and I_{g2} to zero. In this stage, switches $S6$ and $S7$ operate in the same manner as in the peak-value superposition mode, producing the high-frequency current component I_{pp}. The high-frequency currents generated during both intervals are combined with the low-frequency pulse current, yielding the final composite output current I_{out}.

3.3 Control System

The control system is implemented on a STM32G474VE microcontroller, which incorporates a high-performance Arm® Cortex®-M4 32-bit RISC core operating at up to 170 MHz. This architecture provides the real-time processing capability necessary for precise and reliable welding control. In addition, the integrated Memory Protection Unit (MPU) offers dual-layer protection to enhance performance and operational reliability. By establishing a secure and isolated runtime environment, critical control tasks are safeguarded from interference by non-critical functions, preventing program anomalies or memory access violations. This ensures the long-term stability and safe operation of the welding power supply in industrial applications.

To meet the diverse requirements of the welding system, a complete set of peripheral circuits has been developed, including modules for signal sampling and feedback, gate drive control, overvoltage protection, and system communication. These circuits are organized into three subsystems - control, communication, and welding robot control - which operate in coordination to ensure reliable system performance, as illustrated in Fig. 6. A key advantage of the digital implementation is modularity: each subsystem can be independently configured, upgraded, or scaled, greatly enhancing system flexibility and maintainability.

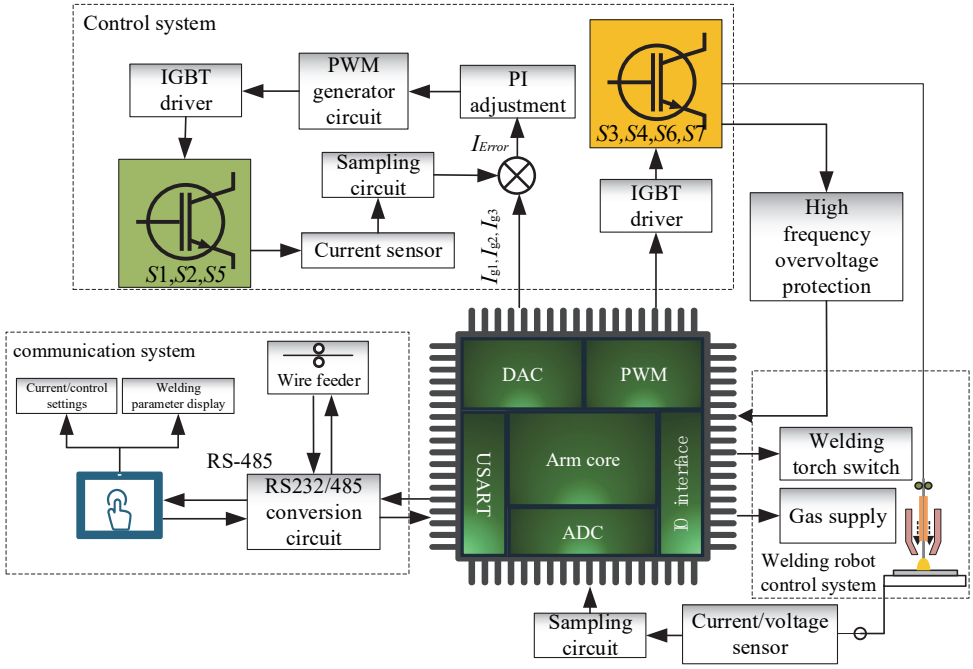

Figure 6 Welding power supply control system

The MCU integrates three dedicated 16-bit PWM timers. According to the configured switching frequency and duty cycle, the generated PWM signals are transmitted through a high-speed optocoupler to the gate drive module, enabling real-time control of IGBT switching and effective modulation of the high-frequency output waveform. In addition, the current reference computed by the control algorithm is output as a digital signal and converted by the on-chip digital-to-analog converter (DAC) into a proportional analog voltage. This voltage serves as the reference for the current loop in the subsequent control stage, directly determining the instantaneous target current of each channel. Through this configuration, precise current regulation is achieved, ensuring both stability and fast response of the welding power supply. The digital signal chain from reference generation to analog actuation highlights the system's capability for real-time monitoring and fine-grained control.

The UART interface is employed to establish communication between the touchscreen and the wire feeder. The welding system adopts a distributed communication architecture consisting of the microcontroller unit (MCU), the human-machine interface (HMI), and the wire feeder execution unit. To suppress electromagnetic interference inherent in welding environments, an external RS485 transceiver circuit is integrated to ensure signal integrity. These three components are interconnected in a daisy-chain configuration via differential RS485 industrial communication, enabling reliable data transmission and efficient system coordination. Through the touchscreen interface, users can monitor the welding process in real

time, adjust parameters dynamically, and configure peripheral devices such as the wire feeder. All user inputs and operational commands are transmitted to the MCU, which serves as the primary communication node, coordinating and managing the overall control tasks of the system. The MCU interprets user commands received from the touchscreen interface and issues corresponding control instructions to downstream slave devices such as the wire feeder. This architecture enables a hybrid control strategy that combines centralized management with distributed execution to coordinate the overall welding process.

For time-critical operations, including the welding gun switch and gas supply solenoid valves, the MCU interfaces directly through general-purpose I/O (GPIO) ports. This direct-drive configuration eliminates the need for additional driver circuits, thereby simplifying the hardware design while ensuring rapid system response.

In the sampling and feedback circuit, isolation amplifiers are employed to separate the high-power domain from the control circuitry, thereby improving both system safety and noise immunity. Combined with the MCU's 16-bit analog-to-digital converter (ADC), this architecture enables high-precision, real-time monitoring and visualization of welding parameters. The sampling stage integrates accurate signal acquisition, voltage-follower buffering, and low-pass filtering to provide clean and stable feedback signals for subsequent processing. These signals are compared through proportional–integral (PI) operational amplifier circuits to achieve accurate closed-loop regulation. In addition, the protection module monitors high-frequency voltage transients across the IGBT switching devices. Leveraging the MCU's external interrupt capabilities and fast computational performance, the system responds rapidly to abnormal conditions, ensuring operational safety and reliability of the welding power supply under dynamic load conditions. The integration of monitoring, feedback, and protection within a unified digital platform further underscores the system's advantages in terms of safety, adaptability, and long-term reliability.

3.4 PI Adjustment

The welding arc, as the actual load of the power supply, exhibits highly nonlinear and time-varying electrical characteristics. During welding, the equivalent arc impedance undergoes rapid, irregular fluctuations caused by operator technique - such as arc length variation and torch oscillation - as well as dynamic physical processes like droplet transfer. Consequently, the output load of the power supply is subject to instantaneous disturbances, posing a major challenge to the dynamic response capability of the control system.

To address these control challenges, a proportional-integral (PI) [26] operational amplifier circuit is employed, a scheme widely adopted in industrial analog control systems. As shown in Fig. 7, the circuit combines proportional amplification and integral computation to achieve precise feedback regulation. The proportional term provides immediate correction based on the instantaneous error magnitude, while the integral term accumulates residual errors over time, ensuring elimination of steady-state deviations. Through this mechanism, the system output converges accurately to the reference value, thereby improving steady-state performance and enhancing control precision of the welding power supply. PI control circuits are commonly implemented using analog operational amplifier configurations. A standard PI controller circuit consists of two fundamental components: the proportional term and the integral term. The proportional term is typically realized using a resistor, which produces an output voltage that is directly proportional to the instantaneous error signal. PI control circuits are typically realized using analog operational amplifiers, with proportional and integral terms implemented through simple resistor-capacitor networks. The proportional branch generates an output directly scaled to the instantaneous error, enabling rapid correction, while the integral branch accumulates the error over time to eliminate steady-state deviations. This compact analog configuration provides a practical and reliable solution for feedback regulation in welding power supplies.

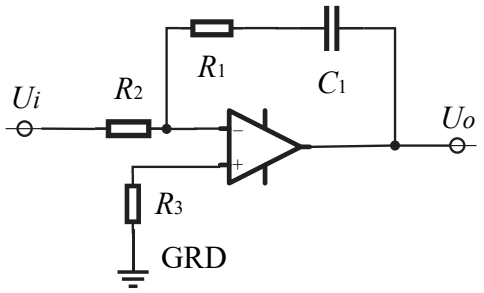

Figure 7 Classic PI circuit

As outlined earlier, the control strategy for regulating the welding power supply output current relies on comparing the reference signal I_g, generated from the MCU setpoint, with the actual feedback signal I_f. The resulting error is processed by a PI controller to achieve closed-loop regulation of the output characteristics. In this work, a dedicated PI circuit is implemented with I_g and I_f as inputs. The circuit, illustrated in Fig. 8, provides real-time correction of current deviations, thereby enhancing both dynamic accuracy and overall system stability.

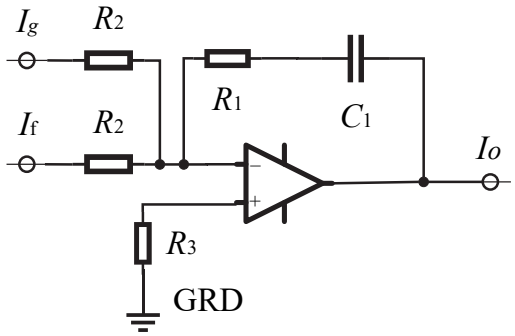

Figure 8 Improved PI control circuit

The time domain equation for the input and output of the new PI operation circuit is as follows. The gain of the proportional term K_p is $-\frac{R_1}{R_2}$, The gain of the integral term K_I is $-\frac{1}{R_2 C_1}$.

$$I_o(t) = -\frac{R_1}{R_2}(I_g(t) + I_f(t)) - \frac{1}{R_2 C_1}\int (I_g(t) + I_f(t))\mathrm{d}t \quad (1)$$

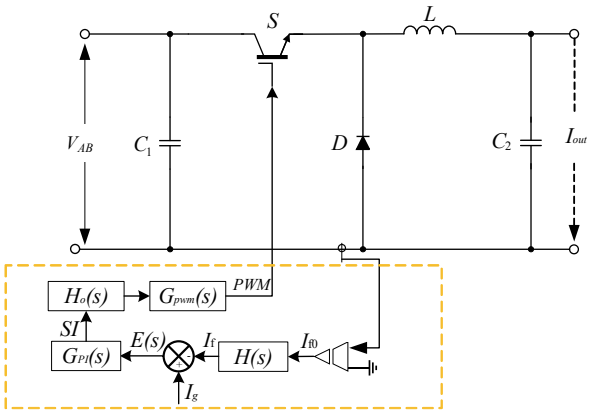

Figure 9 Control system diagram

The control system architecture of the power supply is illustrated in the corresponding Fig. 9. In this system, I_{f0} denotes the output current signal acquired by the Hall-effect current sensor. This signal is processed through the current feedback measurement network, characterized by the transfer function $H(s)$, yielding the feedback current signal I_f. The reference current signal I_g, generated from the MCU setpoint, is compared with I_f to produce the error signal E(s), which serves as the input to the PI regulator. The PI regulator, represented by the transfer function $G_{PI}(s)$, processes this error to generate the current regulation signal SI. This signal is then amplified through the drive circuit with transfer function $H_o(s)$, and subsequently modulated by the PWM generation block, described by the transfer function $G_{pwm}(s)$, to produce the final PWM control signal for driving the IGBT in the Buck converter stage.

Using the Simulink toolbox in MATLAB, both the electrical structure and the control system of the converter were modeled and simulated [27, 28]. Under the proposed control strategy, PWM signals were generated to drive the switching transistors, allowing evaluation of the current response with respect to speed and stability. This simulation process was further employed to determine suitable PI control parameters. The corresponding electrical model is shown in Fig. 10a. Since the rectified front-end circuit provides a constant voltage of approximately 105 V, a constant voltage source is used in its place. The subsequent Buck circuits are constructed using a modular drag-and-drop approach, while the arc load at the output terminal is simplified as a resistive load. This approach enables effective testing of the control system under representative operating conditions and supports subsequent stability analysis and parameter optimization.

The output current is measured using an ammeter module and fed back to the control circuit, as illustrated in Fig. 10b, to realize closed-loop regulation. To generate the low-frequency pulse current during simulation, a pulse generator is added to the "Constant Value" module via a summation block. The pulse generator outputs signals with a defined frequency and duty cycle. During the pulse interval, this signal is superimposed on the base value from the "Constant Value" module to produce the peak signal, while at other times only the base value is applied. This process effectively simulates the generation of the low-frequency pulsed current. The resulting signal is then regulated in closed loop with the feedback current measured from the ammeter module. MATLAB provides built-in PI regulator and PWM modulation tools, enabling automatic duty cycle adjustment according to the PI controller output. This configuration allows the PWM signal, operating at a fixed frequency of 20 kHz, to directly drive the IGBT within the simulation environment. The reference signal I_g is generated by a waveform generator, where the pulse durations T_b and T_p are defined by adjusting the generator's pulse width settings.

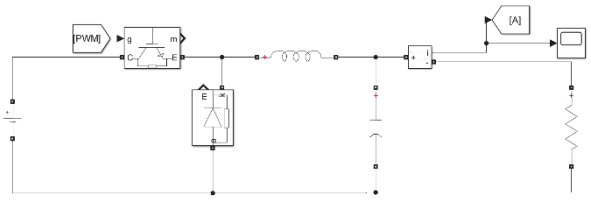

(a) Electrical simulation model

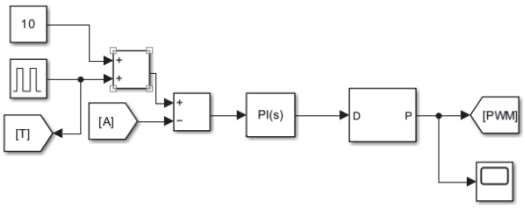

(b) Control system simulation model

Figure 10 MATLAB/Simulink simulation model

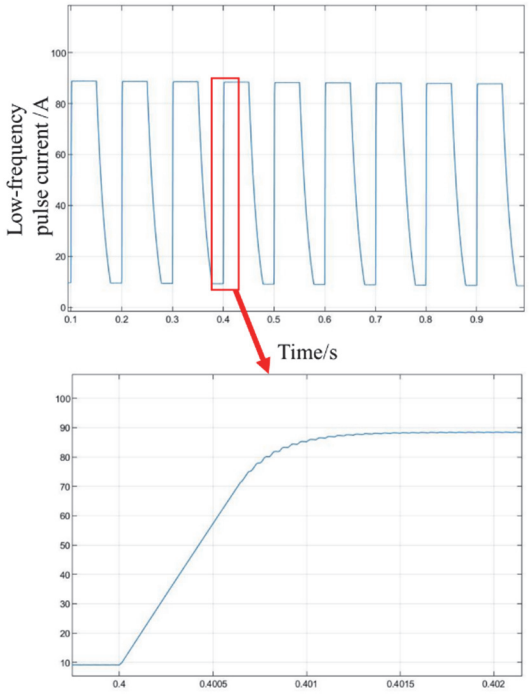

Figure 11 Low-frequency current simulation

Following simulation testing and verification, the PI control parameters were finalized as $K_p = 0.05$ and $K_I = 0.01$. The low-frequency pulse current parameters were set to T_b = 50 ms, T_p = 50 ms, I_b = 10 A and I_p = 90 A. The corresponding simulated current waveform is shown in Fig. 11. With these PI control parameters, the developed power control system exhibits excellent dynamic performance, achieving a current response rate of up to 80 A/ms. During

low-frequency pulse current testing, the system produces a stable output that closely follows the predefined waveform in both amplitude and frequency. The waveform also displays a distinct asymmetry: while the rising edge is sharp, the falling edge shows a slower decay. However, this characteristic arises from the intrinsic behavior of the Buck converter topology, where the output inductor releases stored energy through the freewheeling diode after IGBT turn-off, resulting in a reduced current decay rate.

3.5 Software Design

To ensure efficient and stable operation of the welding power supply while supporting future maintenance, functional upgrades, and code reusability, the control system adopts a modular software architecture. The overall program is partitioned into independent functional modules with clearly defined interfaces, enabling flexible task scheduling and streamlined Modbus-based communication. This modular design enhances adaptability and scalability, providing a robust foundation for precise and flexible welding control. As illustrated in Fig. 12, the software is organized into functional modules including high-frequency pulse control, welding task management, ADC, Modbus communication, and interrupt handling. Among these, the welding task and high-frequency pulse control modules form the system core, coordinating process sequencing and implementing predefined waveform strategies and current parameters.

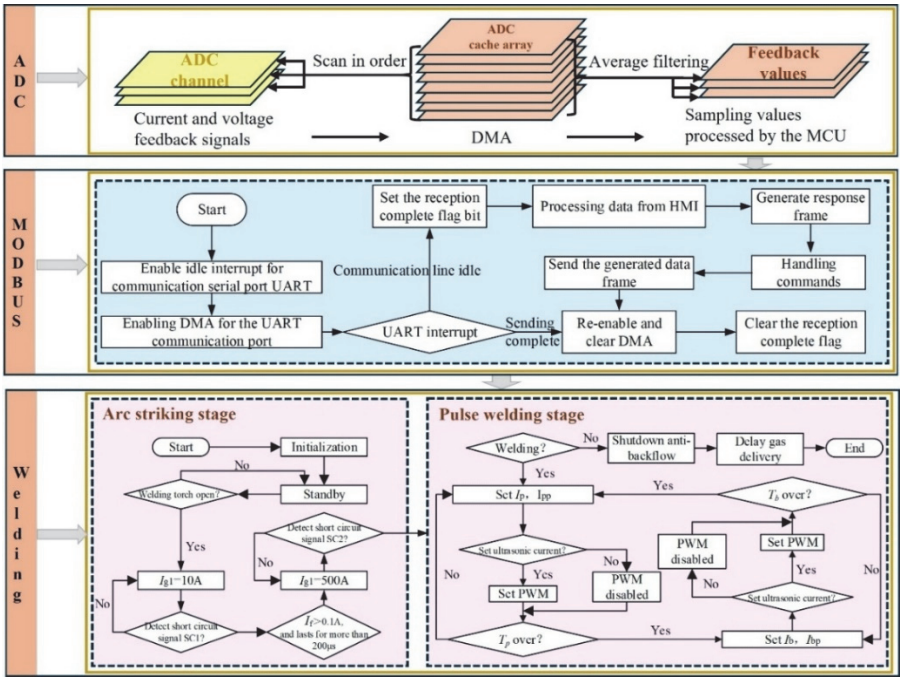

Figure 12 Welding power supply software flowchart

In the ADC process, the MCU integrates its ADC with a DMA controller and interrupt handler to achieve seamless, low-overhead data acquisition. Conversion results are automatically transferred to SRAM, reducing CPU load and reserving resources for core welding control. An averaging filter is applied to the sampled signals to ensure reliable current and voltage feedback. For communication, a Modbus-based query-response scheme is implemented over the RS485 interface, enabling real-time HMI interaction, process monitoring, and parameter adjustment.

To enable precise control over complex welding sequences, the system adopts a cooperative task scheduling strategy based on timer interrupts. A dedicated hardware timer is configured within the welding power supply to generate interrupt signals at fixed intervals of 50 μs. Within the associated interrupt service routine (ISR), multiple software-based counter variables are maintained. By incrementing or decrementing these counters at each interrupt cycle, flexible software timers with resolutions ranging from milliseconds to several seconds are implemented. When a counter reaches its predefined threshold, the corresponding welding state transition or event is triggered, enabling deterministic and time-resolved control of the welding process. This timer-driven scheduling mechanism allows for fine-grained coordination of operations such as arc initiation, waveform switching, duty cycle modulation, and protection logic activation, thereby enhancing the reliability and responsiveness of the control system.

Following power-on initialization, the system enters standby mode, continuously monitoring the I/O port for the welding gun switch status. Once a trigger signal is detected, the gas valve is activated to provide pre-flow, and the low-frequency Buck circuit is enabled in preparation for arc initiation. The power supply employs a contact-based short-circuit ignition method. When the MCU detects the initial short circuit between the welding wire and the workpiece, the system immediately enters the hot-start phase, applying an elevated current to rapidly melt the wire and establish the arc. Successful ignition is confirmed by the transition to a stable short-circuit-arc cycle. Subsequently, the welding current is increased gradually by ramping the current setpoint in software, effectively suppressing inrush current during startup.

During normal welding operation, waveform superposition is executed according to the predefined strategy, with current parameters dynamically adjusted in real time. When ultrasonic current superposition is active,

the voltage across the high-frequency switching transistor is continuously monitored. If this voltage exceeds 400 V, the hardware protection circuit immediately issues a fault signal to the MCU, forcing the high-frequency PWM output into a safe shutdown state. The absorption and feedback circuit absorbs the excess energy, reducing the transistor voltage. Once the voltage returns to a safe level, the fault signal is cleared and the MCU automatically resumes high-frequency PWM operation. This mechanism enables rapid protection and autonomous recovery without operator intervention. Upon deactivation of the welding gun input, the system enters the arc extinction phase, where the output current is gradually reduced and shielding gas flow is extended to protect the weld. The system then returns to standby mode.

4 RESULTS AND DISCUSSION

The list of components for the power supply is detailed in Tab. 1.

Table 1 Experimental specifications

Parameters	Value	Specifications
Input Voltage	380 V	AC
Output Voltage	20-30 V	DC
Output Current	0-500 A	Pulsating direct current
Capacitor	22000 μF-160 V×8	Aluminium electrolytic capacitor
IGBT	FF300R12KS4/ FF150R12KS4	Dual IGBT module

The unit is designed for an output current range of 0-500 A and an output voltage range of 20-30 V. The voltage from the preceding full-bridge rectifier serves as the input for the subsequent output stage. To ensure stability, this input is filtered by eight 22000 μF electrolytic capacitors, each with a voltage rating of 150 V. The output stage utilizes Infineon IGBTs, models FF300R12KS4 and FF150R12KS4.

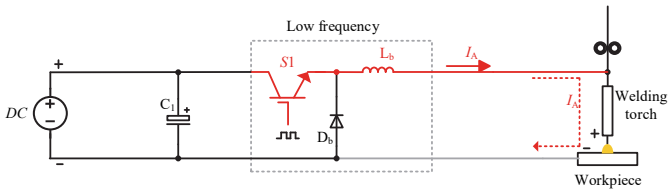

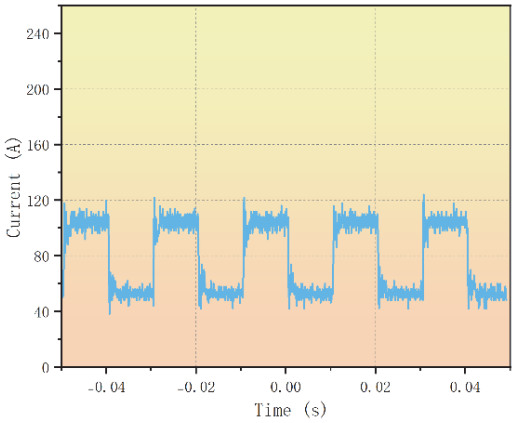

(a) Low-frequency pulse mode

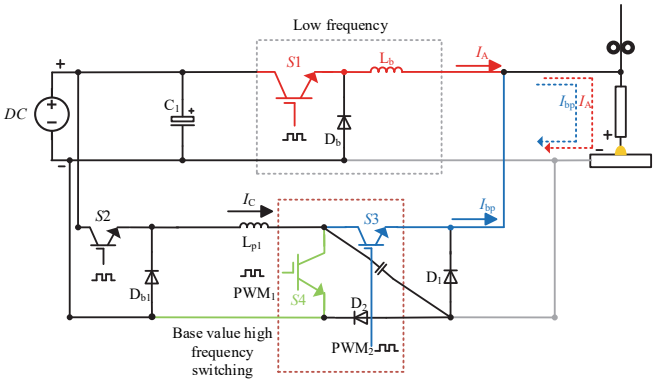

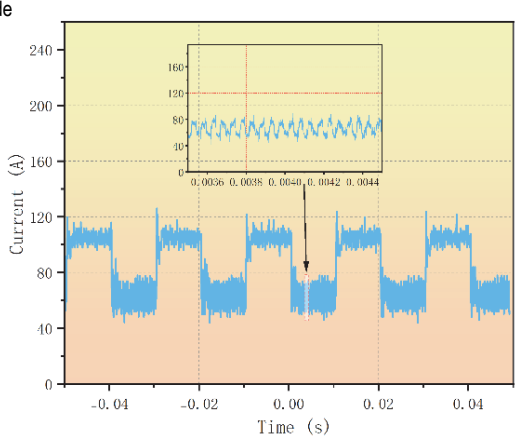

(b) Base value stage superposition mode

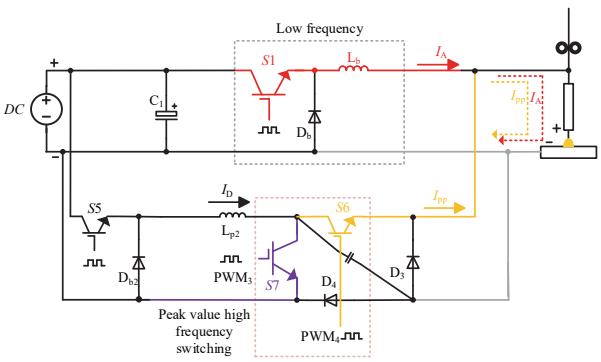

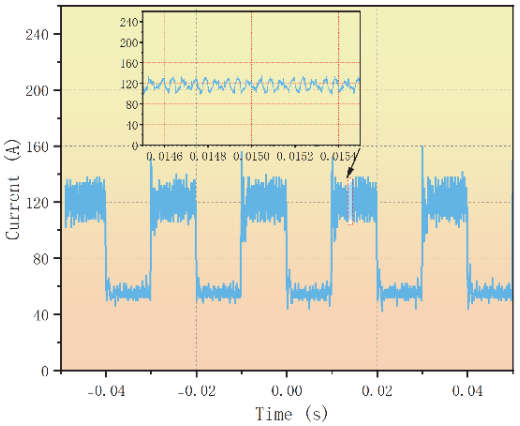

(c) Peak value stage superposition mode

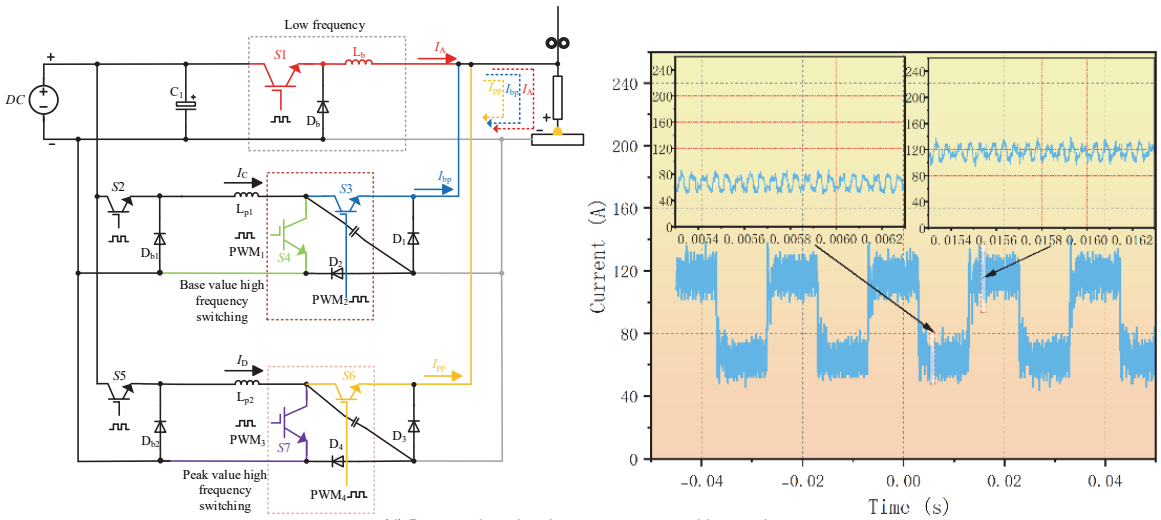

(d) Base and peak value stage superposition mode

Figure 13 Experiment waveforms

To test the external characteristics of the power supply under its various operating modes, it was connected to a resistive load bank. The output current was measured by a Hall effect current sensor (model LT508) connected in series with the output cable. A Tektronix TPS2024B oscilloscope was used to capture the corresponding waveforms.

In Low-frequency pulse mode, the current parameters were set to a base current (I_b) of 60 A and a peak current (I_p) of 120 A, with the corresponding time intervals (T_b and T_p) both set to 10 ms. As illustrated in the corresponding Fig. 13a, output low-frequency pulse current demonstrates the ability to alternate effectively between the set base and peak values. The current at each stage remains stable, and both the rising and falling edges exhibit an excellent dynamic response.

Fig. 13b also shows the result for the Base value stage superposition mode. In this configuration, a high-frequency current (I_{bp}) with parameters of 20 A, 20 kHz, and a 50% duty cycle is superimposed onto the base value stage of the low-frequency current. Observation of the collected waveform confirms that the high-frequency current is successfully superimposed during the base value phase, and the output frequency achieves the required 20 kHz setpoint. Likewise, Fig. 13c illustrates superposition of the high-frequency current onto the peak value stage. When the same high-frequency current parameters were applied during the peak phase (I_{pp}), observation of the waveform confirmed that the superimposed current also reached the predetermined set values.

Finally, the Base and peak value stage superposition mode was tested, with the resulting waveform presented in Fig. 13d. This mode facilitates the independent adjustment of the high-frequency current superimposed onto both the base and peak value stages (I_{bp} and I_{pp}). For the test depicted, the current parameters applied to each respective stage were identical to those used in the previous tests.

Compared with conventional pulsed MIG power supplies, the developed system introduces an additional ultrasonic-frequency current (20-100 kHz) superimposed on both the base and peak phases of the low-frequency current. This capability may enhance droplet transfer stability, reduce spatter, and improve heat input control beyond what is achievable with traditional pulsed supplies. Furthermore, unlike recently reported SiC-based welding machines [24], which rely on wide-bandgap devices to achieve high-frequency operation, the proposed design demonstrates that similar or even higher-frequency ultrasonic currents can be realized using conventional IGBT technology. This highlights both the practicality and cost-effectiveness of the system, offering a viable solution for next-generation welding applications that demand high efficiency and flexible waveform modulation.

5 CONCLUSION

This study developed and tested an ultrasonic-assisted MIG welding power supply integrating a digitally regulated full-bridge inverter and Buck converter topology. The following conclusions can be drawn:

The proposed system successfully generates low-frequency pulsed currents up to 500 A and superimposed ultrasonic currents up to 100 A within the 20-100 kHz range. An innovative absorption and feedback circuit ensures waveform stability and protects IGBTs under high-frequency switching.

The STM32-based digital control system with PI regulation achieves precise current modulation and stable arc behavior. MATLAB/Simulink simulations provided effective parameter optimization, and experimental tests confirmed accurate waveform reproduction.

The system offers improved droplet transfer stability, reduced spatter, and controllable heat input, making it a viable solution for high-efficiency MIG welding applications. Future research will focus on investigating the influence of ultrasonic current superposition on arc stability, droplet transfer, and weld quality under various industrial conditions.

6 REFERENCES

[1] Yuhao Z., Hui C., Ce Y., Jujin H., & Xu Z.(2022). Influence of Laser Power on Droplet Transfer Behavior and Spatter in Laser-MIG Hybrid Welding of Aluminum Alloy. *Laser & Optoelectronics Progress*, *59*(17), 1714005. https://doi.org/10.3788/LOP202259.1714005

[2] Xing, H. R. (2024). Optimizing Human-Machine Systems in Automated Environments. *International Journal of Simulation Modelling*, *23*(4), 716-727. https://doi.org/10.2507/IJSIMM23-4-CO19

[3] Ahsan, Md. R. U., Cheepu, M., Ashiri, R., Kim, T.-H., Jeong, C., & Park, Y.-D. (2017). Mechanisms of weld pool flow and slag formation location in cold metal transfer (CMT) gas metal arc welding (GMAW). *Welding in the World*, *61*(6), 1275-1285. https://doi.org/10.1007/s40194-017-0489-y

[4] Cao, R., Yu, G., Chen, J. H., & Wang, P.-C. (2013). Cold metal transfer joining aluminum alloys-to-galvanized mild steel. *Journal of Materials Processing Technology*, *213*(10), 1753-1763. https://doi.org/10.1016/j.jmatprotec.2013.04.004

[5] Chen, C., Fan, C., Lin, S., Cai, X., Zhou, L., Ye, S., & Yang, C. (2018). Effect of ultrasonic pattern on weld appearance and droplet transfer in ultrasonic assisted MIG welding process. *Journal of Manufacturing Processes*, *35*, 368-372. https://doi.org/10.1016/j.jmapro.2018.08.019

[6] Chen, H., Xue, J.-X., & Heng, G.-C. (2017). A novel sine wave modulation method of pulse current during double wire MIG welding. *The International Journal of Advanced Manufacturing Technology*, *90*(9), 3025-3036. https://doi.org/10.1007/s00170-016-9637-6

[7] Chen, Y., Chen, C., Gao, M., & Zeng, X. (2016). Achieving High Strength Joint of Pure Copper Via Laser-Cold Metal Transfer Arc Hybrid Welding. *Metallurgical and Materials Transactions A*, *47*(6), 2866-2874. https://doi.org/10.1007/s11661-016-3497-4

[8] Da Silva, L. J., Souza, D. M., De Araújo, D. B., Reis, R. P., & Scotti, A. (2020). Concept and validation of an active cooling technique to mitigate heat accumulation in WAAM. *The International Journal of Advanced Manufacturing Technology*, *107*(5-6), 2513-2523. https://doi.org/10.1007/s00170-020-05201-4

[9] Elrefaey, A. & Ross, N. G. (2015). Microstructure and Mechanical Properties of Cold Metal Transfer Welding Similar and Dissimilar Aluminum Alloys. *Acta Metallurgica Sinica*, *28*(6), 715-724. https://doi.org/10.1007/s40195-015-0252-6

[10] Furukawa, K. (2006). New CMT arc welding process - welding of steel to aluminium dissimilar metals and welding of super-thin aluminium sheets. *Welding International*, *20*(6), 440-445. https://doi.org/10.1533/wint.2006.3598

[11] Lei, Z., Li, B., Bi, J., Zhu, P., Lu, W., & Liu, J. (2019). Influence of the laser thermal effect on the droplet transfer behavior in laser-CMT welding. *Optics & Laser Technology*, *120*, 105728. https://doi.org/10.1016/j.optlastec.2019.105728

[12] Pang, J., Hu, S., Shen, J., Wang, P., & Liang, Y. (2016). Arc characteristics and metal transfer behavior of CMT + P welding process. *Journal of Materials Processing Technology*, *238*, 212-217. https://doi.org/10.1016/j.jmatprotec.2016.07.033

[13] Pressman, A. I., Billings, K. H., & Morey, T. (2009). *Switching power supply design* (3rd ed). McGraw-Hill.

[14] Scotti, F. M., Teixeira, F. R., Silva, L. J. D., De Araújo, D. B., Reis, R. P., & Scotti, A. (2020). Thermal management in WAAM through the CMT Advanced process and an active cooling technique. *Journal of Manufacturing Processes*, *57*, 23-35. https://doi.org/10.1016/j.jmapro.2020.06.007

[15] Srinivasan, D., Sevvel, P., John Solomon, I., & Tanushkumaar, P. (2022). A review on Cold Metal Transfer (CMT) technology of welding. *Materials Today: Proceedings*, *64*, 108-115. https://doi.org/10.1016/j.matpr.2022.04.016

[16] Sun, Q., Li, J., Liu, Y., Jiang, Y., Kang, K., & Feng, J. (2018). Arc characteristics and droplet transfer process in CMT welding with a magnetic field. *Journal of Manufacturing Processes*, *32*, 48-56. https://doi.org/10.1016/j.jmapro.2018.01.017

[17] Yao, P., Xue, J., Zhou, K., Wang, X., & Zhu, Q. (2016). Symmetrical transition waveform control on double-wire MIG welding. *Journal of Materials Processing Technology*, *229*, 111-120. https://doi.org/10.1016/j.jmatprotec.2015.08.031

[18] Yi, J. (2015). Effect of welding current on morphology and microstructure of Al alloy T-joint in double-pulsed MIG welding. *Transactions of Nonferrous Metals Society of China.* https://doi.org/10.1016/S1003-6326(15)63953-X

[19] Zhang, P., Liu, Z., Yan, H., & Yu, Z. (2021). Effect of Longitudinal Magnetic Field on CMT Welding of Al-Alloy. *Metals and Materials International*, *27*(12), 5285-5298. https://doi.org/10.1007/s12540-020-00932-1

[20] Gongchun, H., Chen, H., & Xue, J. (2016). Wave control method of twin wire two sine MIG welding. *Welding & Joining*, *5*, 74-75.

[21] Wang, Z., Tang, J., Pan, X., Rao, J., Lin, S., & Xu, M.(2022). Digital High-power AC-Pulse Submerged Arc Welding Power Source. *Journal of Mechanical Engineering*, *59*(2), 96-103. https://doi.org/10.3901/JME.2023.02.096

[22] Wang, Z., Tang, J., Luo, B. et al. (2021). Research on waveform control strategy of high-power pulse-square wave submerged arc welding power supply. *Electric Welding Machine*, *51*(7), 1-5.

[23] Wang, Z., Zhang, F., Wang, P., & Zhang, Q. (2017). Research on full digital robot VPPA welding power supply. *Transactions of the China Welding Institution*, *38*(7), 5-8.

[24] Wang, Z., Jia, J., Hu, J., Liao, H., Wu, J., & Zhang, Q. (2024). Research on local dry underwater fast-frequency pulsed MIG welding power supply. *Transactions of the China Welding Institution, 45*(4), 13-19.

[25] Rao, J., Wu, J., Jiang, D., Tang, J., & Wang, Z. (2021). Development of pulse variable polarity welding power source based on SiC modules. *Transactions of the China Welding Institution*, *42*(7), 21-27.

[26] Ban, L. (2024). An Optimization Approach for Energy Management of Hybrid Vehicles Based on Dynamic Programming and Cuckoo Search. *Tehnicki vjesnik-Technical Gazette*, *31* (6), 2146-2155. https://doi.org/10.17559/TV-20231012001022

[27] Bu, W., Ding, Z., Feng, S., Cai, X., Zhang, Y., Yu, X. & Huang, W. (2024). Research on Control Strategy of High-Speed Grid-Connected FESS (Flywheel Energy Storage System) Based on Dual-PWM Converter. *Tehnicki vjesnik-Technical Gazette*, *31*(1), 178-184. https://doi.org/10.17559/TV-20230803000849

[28] Savran E., Karpat E., Karpat F. (2024). GA and WOA-Based Optimization for Electric Powertrain Efficiency. *International Journal of Simulation Modelling*, *23*(4), 599-610. https://doi.org/10.2507/IJSIMM23-4-699

Contact information:

Borui LU
School of Mechanical Engineering and Automation,
Beihang University,
Beijing 100191, China
E-mail: borui4728@buaa.edu.cn

Bojin QI, Professor
(Corresponding author)
School of Mechanical Engineering and Automation,
Beihang University,
Beijing 100191, China
E-mail: qbj@buaa.edu.cn